Kinetic Modeling of Teboroxime Using Dynamic SPECT Imaging of a Canine Model

Anne M. Smith, Grant T. Gullberg, Paul E. Christian and Frederick L. Datz

Department of Radiology, Division of Nuclear Medicine, Medical Imaging Research Laboratory and the Bioengineering Department, University of Utah, Salt Lake City, Utah

The tomographic utility of ^{99m}Tc-labeled teboroxime has been limited because of its fast washout from the heart, which requires rapid data acquisitions that have not been feasible until the recent development of multidetector SPECT systems. **Methods:** Using a three-detector SPECT system to acquire dynamic tomographic data every 10.2 sec, we investigated the potential of modeling the kinetics of teboroxime to develop a sensitive and quantitative measure of cardiac perfusion. Seven studies were performed on four dogs; in three of the studies the LAD artery was occluded. The three-dimensional activity distributions were reconstructed and were corrected for attenuation using a transmission scan. Time-activity curves from the blood and tissue were fit to a two-compartment model with two-way exchange. **Results:** Performing attenuation correction during the reconstruction process affected the washin parameter k_{21} significantly ($p < 0.0001$). The washin parameter k_{21} also decreased significantly ($p < 0.002$) when the LAD was occluded. **Conclusions:** The results indicate that the washin of teboroxime in myocardial tissue (k_{21}) measured using dynamic SPECT imaging and kinetic modeling is an indicator of myocardial blood flow.

Key Words: cardiac SPECT; ^{99m}Tc-teboroxime; kinetic modeling

J Nucl Med 1994; 35:484–495

Teboroxime labeled with ^{99m}Tc initially generated significant interest as a possible replacement for ^{201}Tl as an agent for detecting myocardial ischemia and infarction (*1,2*). Technetium-99m is more desirable than ^{201}Tl because of its better photon energy for gamma camera detection and reduced radiation exposure. This, combined with the rapid extraction and washout of teboroxime, permits the injection of ten times as much radioactivity compared to ^{201}Tl. However, the rapid clearance from myocardial tissue (10–15-min half-life) makes static SPECT imaging impractical (*3–6*). Thus, over the last few years, the interest in using teboroxime clinically has decreased until the more recent development of multidetector SPECT systems.

The higher geometric efficiency of multidetector SPECT systems allows faster tomographic acquisitions making it possible to dynamically image agents like teboroxime which require high temporal resolution. Dynamic SPECT and the use of kinetic modeling techniques can characterize the washin and washout of teboroxime in the myocardial tissue. This characterization allows the three-dimensional estimation of kinetic rate constants, which may prove to be a more sensitive measure of ischemia than visual interpretations of static images.

PET has already utilized dynamic imaging and kinetic modeling to extract kinetic parameters of physiological processes in organ systems (*7–12*). Dynamic PET has demonstrated the ability to obtain regional myocardial blood flow (*13–15*) and regional myocardial metabolism (*16*). The development of dynamic SPECT for measuring myocardial blood flow can draw upon much of the work done in dynamic PET and tracer kinetic modeling and, in particular, the work that has been accomplished in modeling the kinetics of ^{82}Rb (*14,17,18*). This research has shown that a physiologically appropriate, two-compartment model can quantify regional myocardial blood flow using ^{82}Rb and seems to correlate well with blood flow measured with the microsphere technique (*14,18*).

Since the development of ring and multidetector SPECT systems, new interest has been shown in applying the models developed in PET to study the myocardial kinetics of teboroxime and other agents. Studies examining the washout of teboroxime from the heart were first performed on the SPRINT SPECT system by Stewart et al. (*19*). They suggested that dynamic SPECT imaging and kinetic modeling could potentially estimate myocardial blood flow. Later, Nakajima et al. (*20*) were the first to use a commercial three-detector SPECT system to study the washout phase of teboroxime from the heart. No attenuation correction was performed on the data and the washout data were fit to a bi-exponential function to measure reperfusion after an ischemic insult. These dynamic protocols were performed by starting the acquisition 30 sec after the injection of teboroxime, thus missing most of the washin information. Studying the tracer ^{99m}Tc-pertechnetate, Budinger et al. (*21*) were the first to demonstrate that a three-detector SPECT system could acquire tomographic data in sequential 5-sec acquisitions, which would allow the study of the washin as well as the washout kinetics of teboroxime.

Received Feb. 3, 1993; revision accepted Oct. 26, 1993.

For correspondence and reprints contact: Grant T. Gullberg, PhD, Director, Medical Imaging Research Laboratory, AC213 SOM MIRL, University of Utah, Salt Lake City, UT 84132.

Our work (*22*) was the first to demonstrate that a three-detector SPECT system could be used to measure the in vivo tomographic distribution of both the washin and washout kinetics of ^{99m}Tc-teboroxime. Using kinetic modeling techniques, we were able to estimate washin rate constants which are expected to be more sensitive than washout rate constants in the diagnosis of ischemia for two reasons: (1) the compartment model used to estimate the washin and washout parameters incorporated blood flow in the washin parameter, and (2) estimation of the washin parameter will be more accurate because of the higher count rate during the washin phase of the tissue time-activity curve (*23*). The dynamic tomographic protocol presented in this paper called for imaging to begin at the time of teboroxime injection with a tomographic temporal resolution of 10.2 sec. Also, attenuation correction was performed on the dynamic images using a transmission scan to better quantitate the relative three-dimensional distribution of kinetic parameters.

The work presented in this paper applies dynamic SPECT and kinetic modeling techniques to the evaluation of the kinetics of teboroxime in the canine heart. The objectives of this study were to:

1. Determine if the number of counts acquired in 10.2 sec are sufficient to study the kinetics of teboroxime in a canine using a dynamic SPECT protocol.
2. Investigate placement of a three-dimensional region to generate the blood input function.
3. Verify the utilization of a two-compartment model.
4. Evaluate the effects of attenuation.
5. Determine the effects of reduced blood flow on the kinetics of teboroxime.

Our work draws extensively upon the development of dynamic imaging in PET and is a first step towards developing a new and quantitative measure of myocardial perfusion using dynamic SPECT.

MATERIALS AND METHODS

Animal Preparation

Closed- and opened-chest preparations were used on four canine models. One closed-chest study was used initially to determine if dynamic SPECT was technically feasible due to the anticipated low number of detected counts for the temporal resolution needed to observe teboroxime kinetics. In the opened-chest studies, an ischemic model was created to determine if any of the estimated kinetic parameters were able to differentiate normal and ischemic regions. Two studies were performed on each opened-chest dog: a nonoccluded study and an occluded study.

Closed-chest Preparation. One female mongrel dog (21 kg) was anesthetized with sodium pentobarbital (25 mg/kg) and allowed to breath unassisted. An intravenous drip was placed in an antecubital vein in the foreleg and a catheter was placed in the left femoral artery to measure blood pressure. Blood pressure, ECG and temperature were monitored throughout the study.

Opened-chest Preparation. Three mongrel dogs (2 males, 1 female, 20–36 kg) initially sedated with 5 mg/kg of telazol (MWI Veterinary Supplies, Nampa, ID) were given 4 cc of a muscle relaxant (Pancuronium Bromide, Astra Pharmaceutical Products, Inc., Westborough, MA) and were placed on a ventilator breathing O_2 and halothane (1%–10%). The chest was opened at the fourth left intercostal space. The heart was suspended in a pericardial cradle and 10–15 mm of the left anterior descending (LAD) coronary artery was dissected after the first or second diagonal branch. A vascular occluder (In Vivo Metrics, Healdsburg, CA) was placed on the LAD either between the first and second diagonal branch or after the second diagonal branch, and an electromagnetic flow probe (Micron Medical Inc., Los Angeles, CA) was placed proximal to the occluder. Any arterial branches between the flow probe and occluder were tied off. The flow probe was secured in place by suturing the leads to the myocardium. An intravenous drip was placed in an antecubital vein in the foreleg and a catheter was placed in the left femoral artery to measure blood pressure. The lungs were tucked below the heart, the pericardial cradle was left intact and the chest wall was closed. Blood pressure, ECG and temperature were monitored throughout the study.

Data Acquisition

A three-detector SPECT scanner (Prism 3000, Picker International, Bedford Heights, OH) was used to perform the scanning. Each canine's thoracic cavity was secured on the head-holder of the patient bed with the heart in the center of the field of view. The dog with the closed-chest preparation was in the supine position and the dogs with the opened-chest preparation were placed in the right lateral decubitus position. A transmission scan was performed on each canine for 10 min, acquiring 60 projection angles (10 sec/angle) by using a line source placed at the focal line opposite a fanbeam collimator of 50 cm focal length. The line source contained approximately 20 mCi of ^{99m}Tc. The transmission scan was then used to correct the emission images for nonuniform attenuation (see Data Analysis for more details).

The dynamic SPECT imaging was performed using a circular orbit with continuous rotation, high-resolution fan-beam collimators (50 cm focal length) and an energy window of 15% centered at 140 keV. A complete tomographic data set was collected every 10.2 sec and was binned into sixty 64 × 64 projections; therefore, each projection consisted of data collected as the detector rotated 6 degrees. For the purpose of this paper, a tomographic dataset is a full set of 60 projections acquired every 10.2 sec.

The tomographic dataset acquired during the first 10.2 sec was used to determine background activity. At the start of the second tomographic data acquisition (10.2 sec after the start of initial data acquisition), teboroxime with a net activity ranging between 6.63 and 11.76 mCi was given as a bolus injection through an antecubital vein. In the opened-chest dogs, a second study was performed 45 min after the first injection using net activity ranging between 16.5 and 21.41 mCi of teboroxime after completely occluding the LAD. More activity was given in the occluded study to minimize the effect of residual activity left over from the previous study.

Residual activity from the first scan was determined from the first tomographic data set and subtracted from the following tomographic data sets. The residual activity was assumed to be constant throughout the study based on data collected in previous studies (*19,20*) and our own data which showed that the residual activity's half-life (27–73 min) was long enough to make this assumption valid. The dogs were not moved between the scans. The total number of studies performed on the four canine models (one

closed-chest, three opened-chest) was seven (four baseline and three occluded).

Each tomographic data set was reconstructed to form one three-dimensional image. The closed-chest dog was imaged for 30.6 min for a total of 180 tomographic data sets (46 megabytes of projection data). When 15.3 min of data were fit as compared to 30.6 min, the parameter k_{12} changed less than 4% whereas the parameter k_{21} changed less than 2%. Therefore, the opened-chest dogs were scanned for only 15.3 min for a total of 90 tomographic data sets (23 megabytes of projection data).

Data Analysis

The dynamic tomographic data sets were reconstructed into 34 transaxial 64 × 64 matrices using the iterative expectation-maximization (EM) algorithm (*24,25*). An iterative algorithm was chosen to correct for nonuniform attenuation in all studies by using the reconstructed transmission image (*26,27*). The nonoccluded studies were reconstructed both with and without attenuation correction. When attenuation correction was desired, the transmission image was used to weight the projector/backprojector operator when reconstructing the images. Twenty-five iterations of the EM algorithm were used to reconstruct each transaxial slice since no significant difference occurred in the estimated parameters when more than 25 were used. The voxel dimensions were 0.712 cm in the x, y and z directions. The spatial resolution of the attenuation-corrected images (determined from an experimental phantom) ranged from 1.54 cm FWHM in the image's horizontal direction and 1.53 cm FWHM in the column direction at the base of the heart to 1.38 cm FWHM in the row direction and 1.70 cm in the image's vertical direction at the apex of the heart. The three-dimensional images were reformatted to obtain short-axis slices of the heart. Filtering, corrections for scatter, corrections for nonuniform resolution and corrections for partial volume effects were not performed.

All but the first six reconstructed dynamic images were summed together to create a composite image used to identify region of interest (ROI) placement and occluded regions. The first six images were not included in the composite image as these images contained emissions from the bolus as it traveled through the heart. Each short-axis slice was stored as a dynamic file. Each file consisted of the composite image first, followed by the 90 dynamic images.

Placement of ROIs. Tissue and blood ROIs were drawn on the composite short-axis slices. The ROIs were sampled over time using the dynamic SPECT images to generate time-activity curves. Four tissue ROIs were drawn on the left ventricle for a single short-axis slice. The blood ROIs were drawn inside the left ventricular cavity and left atrium, 0.712 cm from the myocardium. The size of the blood ROIs ranged from 0.64 cm^3 to 1.44 cm^3 on a single slice, while the size of the tissue ROIs ranged from 0.86 cm^3 to 4.7 cm^3. A three-dimensional ROI was obtained by adding multiple two-dimensional regions. Background activity (determined from the first 10.2-sec tomographic data set) was subtracted from all curves and these curves were corrected for the physical decay of ^{99m}Tc. Five short-axis slices from each study (both occluded and nonoccluded) were analyzed, for a total of 140 tissue ROIs.

Compartment Model Parameters. The time-activity curves were fit using a program which estimates parameters based on kinetic data (*28,29*). Each data point from the blood and tissue curves represented an accumulation of counts from radioactive emissions over the acquisition time of 10.2 sec. The tissue time-activity curve was fit to:

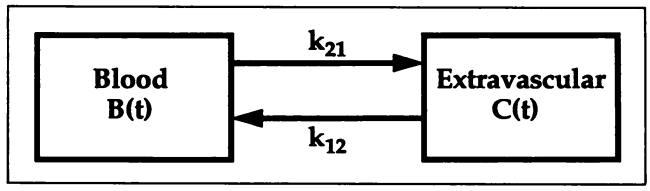

FIGURE 1. Two-compartment model used to fit the dynamic data acquired from imaging teboroxime in the heart. This model assumes first-order kinetics.

$$A(t) = (1 - f_v) \int_{(t-\Delta t)}^{t} C(t)\,dt + f_v \int_{(t-\Delta t)}^{t} B(t)\,dt, \quad \text{Eq. 1}$$

where A(t) represents the model of the measured myocardial tissue activity acquired between the time $t - \Delta t$ and t; f_v represents the vascular fraction of blood in the tissue as well as spillover blood activity into the tissue ROI from the heart chambers due to partial volume and cardiac motion; Δt is the acquisition time of the tomographic dataset; B(t) represents the measured activity in the blood compartment at time t; C(t) represents the activity in the extravascular compartment at time t; and $(1 - f_v)$ represents the fraction of activity emitted from the extravascular compartment. The activity B(t) from the blood compartment was measured using ROIs drawn inside the left intraventricular cavity and left atrium. The activity C(t) from the extravascular compartment is given by the first-order ordinary differential equation:

$$\frac{dC(t)}{dt} = k_{21}B(t) - k_{12}C(t), \quad \text{Eq. 2}$$

which describes the kinetic exchange for the compartment model shown in Figure 1. The parameters k_{21} and k_{12} are the washin and washout rate constants of teboroxime, respectively, and their units are in ml/min/ml of extravascular compartment. The two-compartment model shown in Figure 1 makes the following four assumptions: (1) the time-activity curve of the blood compartment can be measured independently of the extravascular compartment of the myocardial tissue; (2) all myocardial tissue regions exchanged with the same blood time-activity curve; (3) the distribution of the tracer was homogeneous throughout the ROI; and (4) the tissue ROI contained only regions from the blood and extravascular compartments and no regions from outside the heart in the thoracic cavity.

The parameters k_{21}, k_{12} and f_v were estimated in the program by minimizing the Chi-square:

$$\sum_k \frac{(A(t_k) - D(t_k))^2}{\sigma_k^2}, \quad \text{Eq. 3}$$

where $D(t_k)$ are the measured data points from the tissue time-activity curve generated from the reconstructed images. Both the tissue and blood data points were assigned errors, σ_k, which corresponded to the square root of the mean counts obtained from the ROI. The program also estimated the errors of the estimated parameters and calculated a correlation matrix. If the errors from the reconstructed image were used to weight the data points, then the errors would correspond to one standard deviation of the mean. However, obtaining errors from images reconstructed using iterative techniques is extremely difficult. Therefore, the error

bars given by the fitting program were scaled by the factor Chi-square/degrees of freedom, which makes the assumption that the correct model is being used and therefore the Chi-square value of the fit should be approximately equal to the number of degrees of freedom. The distribution volume for each region fit was also calculated by dividing the parameter k_{21} by k_{12}. The fits were considered acceptable by using previously established criteria (*30,31*).

Effects of Attenuation. In the four nonoccluded studies, the images were reconstructed with the EM algorithm (25 iterations) both with and without attenuation correction. The exact same blood and tissue ROIs were drawn on both the attenuation-corrected and uncorrected sets of reconstructions. The effects of attenuation on the kinetic parameters were determined by comparing parameters estimated from attenuation-corrected reconstructions to parameters estimated from uncorrected reconstructions. All three parameters (f_v, k_{21} and k_{12}) were compared by performing a paired two-sample t-test for means, with alpha = 0.05. Differences were considered significant if $p < 0.05$.

To further investigate the effects that attenuation correction had on the dynamic reconstructions, the estimated parameters from the region drawn on the corrected reconstructions were compared to the corresponding region drawn on the uncorrected reconstructions by computing their fractional difference ($diff_P$):

$$diff_P = \frac{(P_{uc} - P_{ac})}{P_{ac}}, \qquad \text{Eq. 4}$$

where P_{uc} is the estimated parameter from the uncorrected dynamic reconstructions and P_{ac} is the estimated parameter from the attenuation-corrected reconstructions.

To determine if the relative attenuation difference between the blood region and a tissue region was causing the difference in the fitted parameters calculated by Equation 4, a measure of the relative attenuation difference was derived. A ratio R_b was calculated between attenuation-corrected blood (B_c) and uncorrected blood (B_{uc}) curves using the equation:

$$R_b = \frac{\int_0^T B_c(t)\,dt}{\int_0^T B_{uc}(t)\,dt}, \qquad \text{Eq. 5}$$

where T is the total length of the scan (15.3 min). Similarly, a ratio R_t was formed between attenuation-corrected tissue (T_c) and uncorrected tissue (T_{uc}) curves:

$$R_t = \frac{\int_0^T T_c(t)\,dt}{\int_0^T T_{uc}(t)\,dt}, \qquad \text{Eq. 6}$$

The measure of the relative attenuation difference between the blood and a tissue region (D_{Rb-Rt}) was derived by taking the fractional difference of R_b and R_t:

$$D_{Rb-Rt} = \frac{R_b - R_t}{R_t}. \qquad \text{Eq. 7}$$

If D_{Rb-Rt} was zero, then the blood and tissue were attenuated equally. If D_{Rb-Rt} was negative, then the tissue was attenuated more than the blood and vice versa if D_{Rb-Rt} was positive.

The fractional difference $diff_P$ for all the parameters (f_v, k_{12} and k_{21}) from all the nonoccluded studies was plotted as a function of D_{Rb-Rt} and a linear regression was performed. A high correlation between $diff_P$ and D_{Rb-Rt} indicates that the change in the estimated parameters from attenuation-corrected reconstructions was caused, in part, by the relative attenuation difference between the blood region and the tissue region.

Effects of Occlusion. Finally, the effects of completely occluding the LAD on the estimated parameters were determined. The tissue regions from the baseline scan in the opened-chest studies were paired off with the corresponding region in the occluded scan. The pairs were then classified as either a nonoccluded pair or an occluded pair by viewing the composite image and determining if the region in question was affected completely or partially by the LAD occlusion. A separate paired two-sample t-test for means ($\alpha = 0.05$) was performed on the nonoccluded pairs and the occluded pairs. Differences were considered significant if $p < 0.05$. Since the opened-chest canines were not moved between scans and the exact same ROIs were drawn for both the baseline and the occluded study, the assumption was made that the size of the heart convolved with the point response of the system, placement of the heart in the scanner, and cardiac motion would affect both studies in the same manner. This assumption allowed a comparison to be made between studies performed on the same canine; however, comparisons of the estimated parameters could not be made between studies performed on different canines.

RESULTS

Data Acquisition

Table 1 shows the data acquisition statistics for all dog studies performed. The %RMS error is in parentheses where appropriate and was calculated by dividing the standard deviation by the mean. Both statistics were calculated using the voxels contained within the drawn ROI. The transmission counts were obtained by summing all the projection data acquired during the transmission scan. To determine the %RMS error for the transmission reconstruction, an ROI was sampled containing the heart. The peak 10.2-sec acquisition counts from the emission studies were determined by summing each dynamic tomographic dataset and choosing the one with the maximum total counts for a 10.2-sec acquisition. The maximum total counts were usually acquired between 10.2 and 20.4 sec after the injection of teboroxime. The total counts acquired over 15.3 min were determined by summing together all the dynamic tomographic data sets that were taken in the first 15.3 min. The statistics for the blood time-activity curves were obtained from selected three-dimensional regions, which were the same regions used when fitting the compartment model to the data. The blood regions included the base of the left ventricle and the left atrium. The tissue time-activity curves were generated from an entire short-axis slice of the left ventricle. The short-axis slice (closer to base than apex) clearly showed the right ventricle. Approximately the same anatomical location was used from each

TABLE 1
Data Acquisition Statistics for all Studies*

	Animal Number						
	P 2464	P 3154		P 3180		P 3231	
	Closed-chest	Unoccluded	Occluded	Unoccluded	Occluded	Unoccluded	Occluded
Transmission counts	53,921,074 (8.2%)	11,196,064 (13.30%)		26,611,592 (9.80%)		38,365,194 (9.10%)	
Net activity administered (mCi/kg)	0.526	0.25	0.623	0.327	0.594	0.523	1.07
Peak 10.2-sec acquisition cts	605,872	391,781	846,933	456,555	873,618	619,135	1,080,160
Total counts acquired over 15 min	41,499,591	19,497,826	53,205,917	18,539,834	44,794,170	29,417,286	78,511,604
Max blood act (cts/cm^3/10.2 sec)†	1044.4 (10.5%)	842.5 (11.2%)	1576 (10.3%)	1188.0 (8.1%)	1793.8 (7.6%)	1363.4 (7.7%)	2045.3 (2.1%)
Max tissue act (cts/cm^3/10.2 sec)†	614.2 (22.0%)	196.9 (30.8%)	569.6 (21.2%)	251.5 (22.4%)	479.5 (20.2%)	298.6 (15.2%)	551.3 (20.1%)

*%RMS error in parentheses and calculated using voxel dimensions.
†Activity curves generated from attenuation-corrected reconstructions.

study to obtain the maximum tissue activity shown in Table 1.

In Table 1, the opened-chest studies' maximum values for the blood and myocardial tissue time-activity curves correlated with the net activity administered. The %RMS error showed some correlation to net activity administered. Although the closed-chest study (P2464) showed similar maximum blood activity relative to net activity administered, it demonstrated significantly higher maximum tissue uptake.

For the first studies (baseline) performed on each canine, background counts were 0 in the reconstructed heart regions. For the second studies (occluded) performed on each canine, background counts (due to the residual activity from the first scan) in the myocardium ranged from 11.4% to 15.3% of the peak counts in the tissue time-activity curve, whereas background counts in the blood ranged from 1.78% to 2.76%.

The composite reconstruction from the closed-chest study (P2464), formed by summing the last 29 min of dynamic data, is shown in Figure 2 with a two-dimensional blood region and the myocardial tissue ROIs labeled as 13, 14, 15 and 16. Also, the first 16 unfiltered dynamic reconstructions of one short-axis slice are shown. Each image represents 10.2 sec of acquisition time and the images spanned a time from 0 to 163.2 sec, with 0 being the injection time of teboroxime. Image 1 shows the bolus as it passed through the right side of the heart and the lungs. The following images show decreasing activity in the lungs and increasing activity in the left ventricle and liver as the bolus progressed.

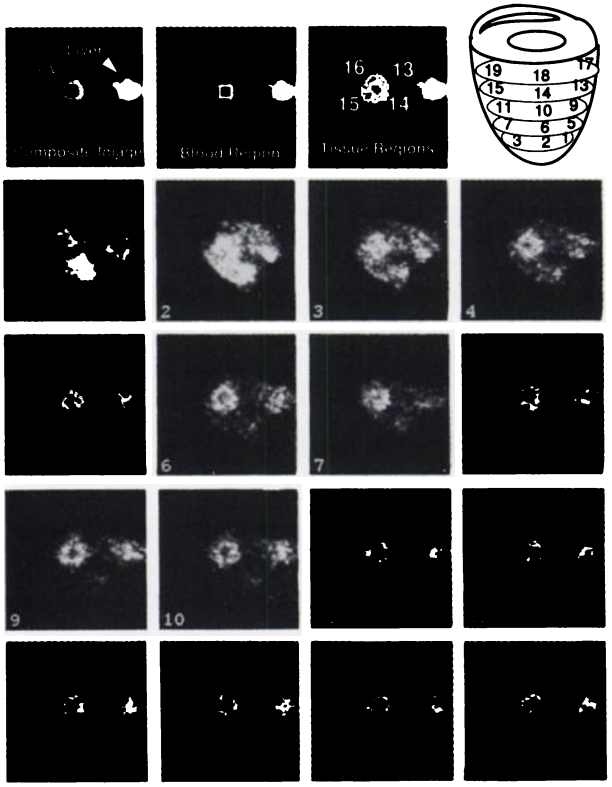

FIGURE 2. Ten-second dynamic SPECT images from the closed-chest study (P2464). This is a short-axis slice of the heart observed over time. The first three images show the bolus progressing through heart chambers and lungs, while subsequent images show myocardial tissue and liver after most of the teboroxime has been extracted from the blood. Image 1 was acquired from 0 to 10.2 sec, with time 0 being the time teboroxime was injected. Image 16 was acquired from 153 to 163.2 sec. Composite images of the same slice are shown at top with blood and tissue ROIs and with a schematic showing how the heart was sliced and the regions labeled. Regions 4, 8, 12, 16 and 20 are the septal wall regions and cannot be seen on the schematic. These regions are the same as those listed in Tables 2 and 3. RV = right ventricle.

Optimal Placement of ROIs

The blood ROIs were defined by analyzing the first three dynamic images and outlining the bolus of teboroxime as it passed through the left side of the heart. In each dog study, blood ROIs were averaged from four or five separate short-axis slices, creating a three-dimensional blood ROI ranging in size from 5.8 to 7.2 cm^3. Blood time-activity curves were generated from the dynamic reconstructions by observing

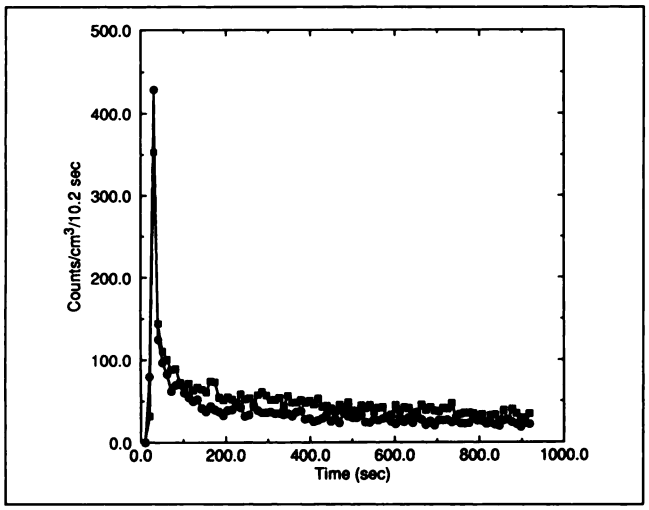

FIGURE 3. Comparison of time-activity curves generated from a three-dimensional ROI drawn in the base of the left ventricle and atrium (●) to a three-dimensional ROI drawn in apical left ventricle (□). The base ROI was 7.22 cm^3 and the apical ROI was 6.5 cm^3.

the same ROI over time. The %RMS error for the maximum ROI activity is shown in Table 1.

Figure 3 shows the comparison of a blood time-activity curve generated from regions located near the base of the heart and a blood time-activity curve generated from a region located near the apex. The region near the base included the top of the left ventricle and left atrium. Note the higher peak and lower tail points in the base region, which indicate less extravascular contamination in the base as compared to the apical region.

When the myocardial tissue ROIs were drawn as shown in Figure 2, care was taken to stay at least one voxel away from the epicardial edge and the endocardial edge of the myocardium to avoid problems caused by cardiac motion between systole and diastole. The ROI boundaries were drawn on the blurred area of the myocardium, and the ROI was sampled inside of this boundary. The heart motion caused the epicardial and endocardial edges to be blurred. Keeping the tissue ROI away from the endocardial edge was not as critical as keeping it away from the epicardial edge, as the parameter f_v (volume fraction of blood activity in the extravascular compartment) modeled the blood activity in the intraventricular cavity included in the tissue ROI. This result was determined using computer simulations (*23*), whereby the parameter f_v increased when extravascular activity was averaged with blood activity, while k_{21} and k_{12} remained relatively constant.

Estimated Parameters

Figure 4 shows a myocardial tissue curve and fit from region 15 in the closed-chest study (Fig. 2). The estimated parameters were: $f_v = 0.388 \pm 0.017$, $k_{21} = 1.75 \pm 0.051$ min^{-1} and $k_{12} = 0.848 \pm 0.025$ min^{-1}. The fitted curve is not smooth because an unfiltered blood curve generated from the reconstructions was used when fitting the data to the compartment model.

Tables 2 and 3 show the estimated parameters with their respective %RMS errors and the distribution volume (calculated by dividing k_{21} by k_{12}) for each canine study. The regions are the same regions as those shown in the schematic in Figure 2. The parameters were estimated from the attenuation-corrected reconstructions in Table 2. All fits converged in 10 iterations or less and were independent of the initial starting values. The average correlations between the various parameters for all studies and fits were: −0.240 (s.d. = 0.076) for k_{12} to f_v, 0.225 (s.d. = 0.239) for k_{21} to f_v and 0.813 (s.d. = 0.076) for k_{21} to k_{12}.

In Table 3, the parameters k_{21} and k_{12} in the closed-chest study were consistently larger as compared to the same parameters from any of the opened-chest studies. This result is consistent with the data in Table 1 which showed that for the closed-chest study, teboroxime had a higher maximum myocardial tissue uptake relative to the maximum blood activity than any of the opened-chest studies. The average value for the distribution volume was 2.36 (s.d. = 0.54 and n = 140), indicating that teboroxime is either bound or nonpermanently trapped in the myocardial tissue.

Effects of Attenuation

Table 3 shows the parameters estimated from the attenuation-corrected images compared to the parameters estimated from the uncorrected images from the closed-chest study. A paired two-sample t-test for means was performed using all the parameters from the nonoccluded studies to determine if attenuation correction affected the fitted parameters significantly. For alpha = 0.05 and n = 80, only the parameter k_{21} showed a significant change ($p < 0.0001$, with a 95% confidence interval of $-0.422 < \mu_1 - \mu_2 < 0.030$).

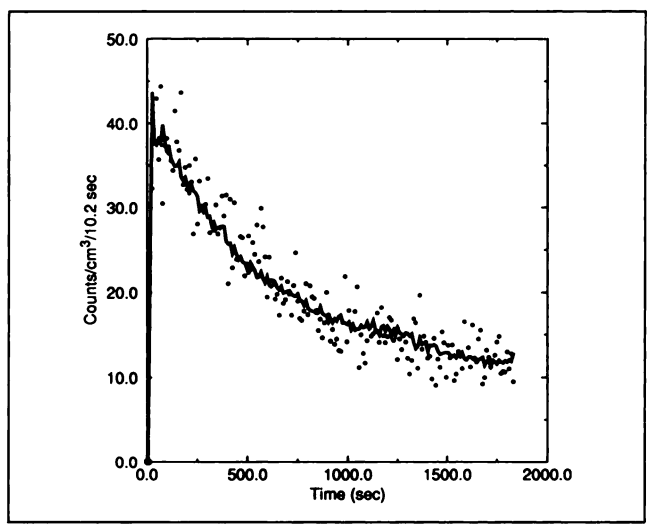

FIGURE 4. A myocardial tissue curve (●) and fit (—) to the two-compartment model shown in Figure 1 for the closed-chest study. Region 15 in Figure 2 was used to generate the tissue activity curve, and its size was 0.93 cm^3. The estimated parameters were: $f_v = 0.388 \pm 0.017$, $k_{21} = 1.75 \pm 0.051$ min^{-1} and $k_{12} = 0.848 \pm 0.025$ min^{-1}.

TABLE 2
Estimated Parameters and Distribution Volume (D.V.) from Attenuation-Corrected Images from Opened-chest Studies*

P3154 opened-chest study								
	Baseline study				Occluded study			
Region	f_v	k_{21} (1/min)	k_{12} (1/min)	D.V.	f_v	k_{21} (1/min)	k_{12} (1/min)	D.V.
1	0.166 (52.6)	0.590 (19.9)	0.229 (24.3)	2.58	0.195 (43.3)	0.464 (18.4)	0.195 (26.8)	2.38
2	0.177 (55.2)	0.439 (23.8)	0.206 (30.6)	2.13	0.121 (47.9)	0.348 (16.4)	0.195 (23.8)	1.78
3†	0.144 (57.6)	0.380 (23.8)	0.216 (30.5)	1.76	0.150 (34.0)	0.326 (13.8)	0.180 (20.9)	1381
4†	0.177 (52.2)	0.422 (24.2)	0.229 (30.3)	1.85	0.390 (47.9)	0.200 (75.0)	0.195 (106.2)	1402
5	0.207 (64.6)	0.652 (28.1)	0.236 (33.2)	2.76	0.230 (47.5)	0.405 (23.2)	0.154 (38.6)	2.64
6	0.184 (62.1)	0.482 (27.8)	0.236 (34.1)	2.04	0.161 (55.1)	0.367 (22.5)	0.190 (33.1)	1.93
7†	0.158 (46.5)	0.388 (20.4)	0.223 (25.9)	1.74	0.303 (21.6)	0.284 (18.1)	0.174 (28.3)	1763
8	0.259 (54.9)	0.474 (30.1)	0.198 (39.1)	2.40	0.256 (32.0)	0.369 (19.0)	0.179 (29.1)	2.07
9	0.267 (35.8)	0.760 (18.8)	0.255 (21.0)	2.98	0.348 (20.2)	0.495 (13.5)	0.163 (21.2)	3.03
10	0.206 (42.6)	0.547 (20.8)	0.257 (24.9)	2.13	0.170 (41.5)	0.403 (17.4)	0.210 (24.4)	1.92
11	0.157 (61.8)	0.435 (25.2)	0.225 (31.7)	1.94	0.232 (40.7)	0.347 (22.6)	0.174 (35.1)	2.00
12	0.389 (42.8)	0.599 (33.3)	0.209 (40.1)	2.87	0.481 (24.6)	0.493 (24.9)	0.187 (36.8)	2.64
13	0.441 (25.6)	0.856 (22.7)	0.272 (23.0)	3.14	0.495 (16.6)	0.657 (15.9)	0.195 (21.1)	3.37
14	0.309 (31.2)	0.598 (20.8)	0.253 (24.5)	2.36	0.300 (23.8)	0.483 (15.1)	0.217 (21.0)	2.23
15	0.201 (50.1)	0.467 (23.9)	0.224 (29.7)	2.08	0.177 (34.3)	0.401 (14.4)	0.197 (20.8)	2.04
16	0.376 (35.2)	0.683 (27.9)	0.273 (31.5)	2.50	0.510 (17.2)	0.586 (18.0)	0.203 (24.6)	2.89
17	0.606 (42.4)	1.109 (60.8)	0.295 (48.9)	3.77	0.700 (30.7)	0.944 (56.5)	0.198 (57.4)	4.77
18	0.385 (46.9)	0.642 (39.7)	0.295 (44.7)	2.18	0.534 (39.6)	0.588 (51.9)	0.289 (67.8)	2.03
19	0.222 (52.0)	0.481 (27.7)	0.252 (33.2)	1.91	0.201 (38.2)	0.360 (19.3)	0.194 (28.3)	1.85
20	0.499 (30.3)	0.691 (34.4)	0.308 (37.3)	2.24	0.563 (14.3)	0.601 (17.5)	0.210 (23.8)	2.87

P3180 opened-chest study								
	Baseline study				Occluded study			
Region	f_v	k_{21} (1/min)	k_{12} (1/min)	D.V.	f_v	k_{21} (1/min)	k_{12} (1/min)	D.V.
1	0.375 (21.4)	0.996 (17.7)	0.383 (17.7)	2.60	0.454 (20.5)	0.999 (21.2)	0.474 (20.9)	2.11
2†	0.178 (31.4)	0.807 (13.9)	0.374 (14.6)	2.16	0.278 (42.3)	0.732 (28.7)	0.460 (30.2)	1.59
3†	0.258 (32.7)	0.698 (20.9)	0.355 (22.5)	1.97	0.481 (20.8)	0.057 (203.7)	0.247 (202.5)	0.23
4	0.303 (41.5)	0.901 (26.3)	0.348 (26.5)	2.59	0.458 (28.5)	0.661 (31.0)	0.369 (32.4)	1.79
5	0.300 (23.9)	0.853 (15.6)	0.349 (16.1)	2.44	0.322 (27.6)	0.924 (18.6)	0.418 (18.6)	2.21
6†	0.195 (27.0)	0.828 (12.6)	0.379 (13.2)	2.18	0.272 (25.2)	0.844 (15.6)	0.449 (16.2)	1.88
7†	0.181 (39.9)	0.720 (18.5)	0.363 (19.8)	1.98	0.332 (27.9)	0.319 (40.6)	0.452 (40.9)	0.71
8	0.349 (37.6)	0.969 (27.0)	0.349 (26.6)	2.77	0.447 (41.3)	1.021 (37.8)	0.398 (34.8)	2.56
9	0.443 (51.1)	1.099 (47.8)	0.382 (44.0)	2.88	0.306 (42.8)	1.031 (27.2)	0.432 (27.4)	2.39
10	0.269 (60.5)	0.896 (34.0)	0.396 (34.3)	2.26	0.206 (39.8)	0.943 (18.1)	0.444 (18.6)	2.12
11†	0.226 (41.6)	0.787 (22.1)	0.363 (23.4)	2.17	0.411 (22.8)	0.582 (25.3)	0.433 (26.5)	1.34
12	0.379 (38.0)	0.943 (31.7)	0.389 (32.0)	2.42	0.436 (29.4)	0.912 (26.8)	0.386 (26.1)	2.36
13	0.448 (28.9)	1.035 (28.0)	0.376 (26.5)	2.75	0.478 (32.0)	1.125 (32.3)	0.404 (29.6)	2.79
14	0.234 (63.5)	0.796 (31.8)	0.394 (32.8)	2.02	0.272 (34.4)	0.935 (20.5)	0.466 (20.9)	2.01
15	0.212 (48.9)	0.770 (24.4)	0.374 (25.6)	2.06	0.376 (33.9)	0.807 (27.4)	0.405 (27.6)	1.99
16	0.426 (28.5)	1.061 (26.4)	0.402 (25.4)	2.64	0.487 (25.6)	1.159 (26.6)	0.426 (23.9)	2.72
17	0.473 (30.9)	0.905 (32.5)	0.347 (32.1)	2.61	0.490 (29.8)	0.997 (31.3)	0.383 (29.0)	2.60
18	0.192 (64.8)	0.740 (29.9)	0.400 (31.2)	1.85	0.233 (40.5)	0.809 (22.3)	0.443 (23.4)	1.83
19	0.237 (50.1)	0.799 (28.6)	0.400 (30.1)	2.00	0.386 (36.9)	0.889 (29.5)	0.389 (29.2)	2.28
20	0.408 (33.8)	0.956 (31.6)	0.434 (31.7)	2.20	0.545 (71.1)	1.292 (87.6)	0.512 (77.6)	2.52

*%RMS errors in parentheses.
†Regions at least partially affected (by examining composite image) by occlusion of the LAD in the occluded study.

The fractional difference $diff_P$ (calculated using Equation 4) for all three parameters is plotted as a function of D_{Rb-Rt} (calculated using Equation 7) in Figure 5 for the nonoccluded study (P3180). When the linear correlation coefficient (r) was calculated for all nonoccluded studies (n = 4) and all parameters, r ranged from 0.468 to 0.857 for $diff_{fv}$, 0.864 to 0.974 for $diff_{k21}$ and 0.161 to 0.650 for $diff_{k12}$. Thus, the relative attenuation difference between the blood and the tissue regions demonstrated a high correlation to the estimated parameter k_{21}. Also note in Figure 5 that the

TABLE 2A
Estimated Parameters and Distribution Volume (D.V.) from Attenuation-Corrected Images from Opened-chest Studies*

	P3231 opened-chest study							
1	0.328 (50.8)	0.744 (34.0)	0.260 (40.4)	2.86	0.402 (39.4)	0.713 (31.4)	0.245 (34.1)	2.91
2	0.196 (34.2)	0.597 (16.6)	0.258 (20.8)	2.32	0.240 (44.4)	0.632 (22.3)	0.261 (25.4)	2.42
3†	0.240 (38.2)	0.609 (22.8)	0.293 (27.5)	2.08	0.401 (38.4)	0.389 (35.1)	0.195 (45.1)	2.00
4†	0.193 (22.9)	0.697 (10.8)	0.288 (13.0)	2.42	0.315 (26.3)	0.247 (22.1)	0.135 (35.1)	1.84
5	0.374 (28.9)	0.741 (23.0)	0.252 (27.3)	2.93	0.458 (18.9)	0.758 (18.2)	0.250 (19.2)	3.03
6	0.281 (33.8)	0.671 (20.8)	0.250 (25.5)	2.68	0.277 (32.9)	0.728 (18.8)	0.272 (20.9)	2.68
7†	0.281 (35.0)	0.602 (23.9)	0.271 (29.4)	2.22	0.422 (25.0)	0.504 (23.6)	0.221 (28.1)	2.28
8†	0.368 (48.9)	0.785 (37.1)	0.249 (43.1)	3.15	0.417 (26.3)	0.552 (23.0)	0.203 (27.4)	2.72
9	0.464 (23.8)	0.823 (24.1)	0.249 (26.8)	3.30	0.512 (23.9)	0.875 (26.2)	0.246 (26.0)	3.56
10	0.306 (46.8)	0.639 (31.1)	0.257 (38.0)	2.49	0.342 (19.7)	0.742 (14.2)	0.284 (15.5)	2.61
11	0.278 (33.9)	0.649 (22.0)	0.281 (26.5)	2.31	0.401 (15.8)	0.708 (13.4)	0.263 (14.5)	2.69
12	0.370 (46.9)	0.703 (37.0)	0.247 (44.5)	2.85	0.434 (21.4)	0.652 (19.7)	0.234 (22.2)	2.79
13	0.520 (23.8)	0.801 (28.2)	0.237 (31.5)	3.38	0.559 (19.4)	0.829 (24.9)	0.258 (24.6)	3.21
14	0.428 (55.4)	0.699 (50.2)	0.274 (57.8)	2.55	0.447 (25.3)	0.756 (24.5)	0.290 (26.1)	2.61
15	0.354 (17.3)	0.665 (14.1)	0.267 (16.8)	2.49	0.433 (21.2)	0.699 (19.4)	0.260 (20.8)	2.69
16	0.377 (50.2)	0.701 (40.5)	0.260 (47.6)	2.69	0.396 (34.5)	0.722 (29.7)	0.284 (32.9)	2.54
17	0.593 (15.2)	0.703 (23.1)	0.227 (27.3)	3.10	0.622 (16.9)	0.775 (27.5)	0.280 (28.1)	2.77
18	0.402 (44.6)	0.485 (45.2)	0.245 (59.6)	1.98	0.431 (24.2)	0.568 (27.2)	0.314 (30.8)	1.81
19	0.400 (28.7)	0.549 (27.2)	0.241 (34.6)	2.27	0.360 (24.4)	0.605 (20.2)	0.289 (22.9)	2.10
20	0.535 (22.7)	0.738 (29.6)	0.270 (33.8)	2.74	0.532 (21.5)	0.777 (26.6)	0.289 (27.8)	2.69

*%RMS errors in parentheses.
†Regions at least partially affected (by examining composite image) by occlusion of the LAD in the occluded study.

slope of the linear regression lines for $diff_{fv}$ and $diff_{k21}$ is greater than 1.0. This relationship has been verified using computer simulations (*23*).

The above analysis is based on the assumption that only the amplitude of the blood and myocardial tissue curves are affected by attenuation correction, and not the shape. This assumption is made in Equations 5 and 6 when calculating the R_b and R_t ratios. If the shape of the curves

TABLE 3
Comparison of Estimated Parameters (Closed-Chest Study) from Attenuation-Corrected and Uncorrected Images*

	P2464 closed-chest study							
	Attenuation Corrected				Uncorrected			
Region	f_v	k_{21} (1/min)	k_{12} (1/min)	D.V.	f_v	k_{21} (1/min)	k_{12} (1/min)	D.V.
1	0.263 (82.3)	1.975 (36.7)	0.939 (38.3)	2.10	0.087 (137.1)	1.906 (21.7)	0.945 (23.3)	2.02
2	0.389 (62.6)	2.643 (39.5)	1.075 (38.8)	2.46	0.237 (77.9)	2.656 (27.6)	1.100 (28.5)	2.41
3	0.420 (58.7)	2.061 (41.6)	0.969 (40.6)	2.13	0.330 (54.2)	2.700 (26.2)	1.061 (25.3)	2.55
4	0.222 (61.4)	1.735 (25.3)	0.868 (26.7)	2.00	0.247 (46.4)	2.057 (18.9)	0.859 (19.1)	2.39
5	0.371 (71.5)	2.219 (45.0)	0.984 (45.5)	2.25	0.177 (77.4)	2.060 (24.4)	0.996 (25.8)	2.07
6	0.399 (85.7)	2.667 (53.1)	1.027 (47.3)	2.60	0.259 (78.4)	2.599 (29.9)	1.026 (28.9)	2.53
7	0.482 (53.4)	1.993 (46.6)	0.912 (44.4)	2.19	0.422 (50.0)	2.736 (33.4)	0.996 (29.7)	2.75
8	0.306 (58.6)	1.729 (32.4)	0.822 (33.9)	2.10	0.330 (45.1)	2.156 (23.6)	0.849 (23.1)	2.54
9	0.465 (57.3)	2.062 (46.2)	0.841 (40.8)	2.45	0.244 (62.9)	1.933 (25.5)	0.912 (25.9)	2.12
10	0.428 (54.4)	2.763 (38.7)	1.112 (36.0)	2.48	0.339 (45.1)	2.734 (24.1)	1.126 (23.1)	2.43
11	0.437 (48.1)	1.968 (37.9)	0.924 (38.1)	2.13	0.424 (44.3)	2.754 (30.3)	1.032 (28.0)	2.67
12	0.353 (39.4)	1.545 (25.3)	0.727 (25.9)	2.12	0.338 (33.6)	1.877 (18.7)	0.754 (18.4)	2.49
13	0.509 (39.2)	2.365 (37.2)	0.952 (34.9)	2.48	0.321 (37.5)	2.260 (20.9)	1.033 (21.6)	2.19
14	0.529 (48.3)	2.601 (47.6)	1.040 (45.3)	2.50	0.480 (36.8)	2.580 (31.0)	1.043 (29.3)	2.47
15	0.561 (39.3)	2.444 (44.4)	1.057 (41.8)	2.31	0.523 (34.6)	3.134 (32.8)	1.143 (28.2)	2.74
16	0.388 (60.0)	1.754 (40.3)	0.848 (41.2)	2.07	0.445 (49.7)	2.535 (34.3)	0.922 (30.0)	2.75
17	0.534 (50.4)	1.941 (51.0)	0.914 (48.8)	2.12	0.383 (46.3)	2.008 (30.8)	0.998 (31.2)	2.01
18	0.708 (39.7)	3.074 (72.8)	1.065 (57.0)	2.89	0.650 (30.2)	2.854 (43.9)	1.090 (36.5)	2.62
19	0.437 (50.2)	2.034 (43.3)	1.066 (45.4)	1.91	0.561 (41.8)	3.390 (43.6)	1.163 (36.8)	2.91
20	0.428 (56.1)	1.753 (41.7)	0.935 (42.0)	1.87	0.460 (47.6)	2.688 (34.2)	1.027 (28.6)	2.62

*%RMS errors in parentheses.

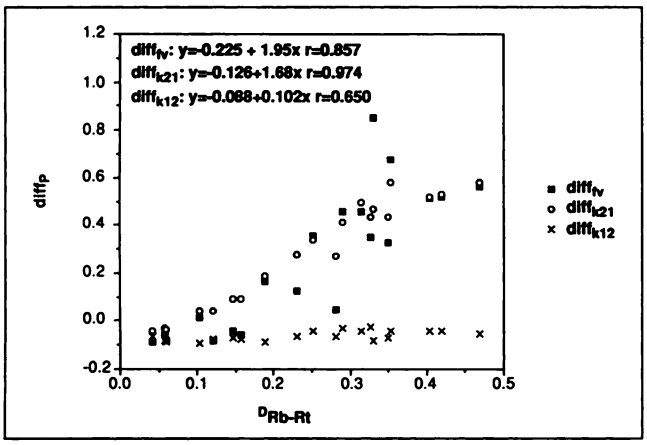

FIGURE 5. Regional variation of fractional difference of parameters $diff_P$ (Equation 4) between uncorrected images and attenuation-corrected images from canine study P3180, plotted as a function of D_{Rb-Rt} (Equation 7), which is a measure of relative attenuation differences between blood and myocardial tissue regions. If $D_{Rb-Rt} = 0$, then they were attenuated equally, if $D_{Rb-Rt} < 0$, then the tissue region was attenuated more than the blood region, and if $D_{Rb-Rt} > 0$, then the blood region was attenuated more than the tissue region. The linear regression with its respective correlation coefficient is also given for each $diff_P$.

changed as well as the amplitude, then D_{Rb-Rt} could not be used as a measure of the relative attenuation difference between the blood and a tissue region. When the attenuation-corrected and uncorrected time-activity curves were normalized to their respective area under the curve, very little difference was seen in the shape of the curves.

Effects of Occlusion

Figure 6 shows the summed short-axis slices of an opened-chest study (P3180) for both the normal and occluded study, along with the plots of k_{21} as a function of slice number for each of the regions. Since the dog was not moved between scans, the slices from the normal study and the occluded study match exactly. The parameter k_{21} decreases in regions 11, 7 and 3, which is where the occlusion defect appears in the composite images.

When the regions from the baseline study were paired off with their corresponding regions from the occluded study and classified as either a nonoccluded pair or an occluded pair, 48 pairs were classified as nonoccluded and 12 pairs were classified as occluded (Table 2). When a paired two-sample t-test for means was performed on both groups, the results showed that there was no significant difference for k_{21} and k_{12} in the nonoccluded group. The p value for f_v was less than 0.0001 for the nonoccluded group, but the 95% confidence interval for this difference was $-0.010 < \mu_1 - \mu_2 < 0.008$ which shows that the magnitude of the difference was so small that it is unimportant. For the occluded group, f_v showed a significant difference with $p < 0.0001$ and a 95% confidence interval of $-0.201 < \mu_1 - \mu_2 < -0.061$. The parameter k_{21} also showed a significant difference for the occluded group with $p < 0.002$ and a 95% confidence interval of $0.045 < \mu_1 - \mu_2 < 0.403$. The change in k_{12} from a baseline region to an occluded region showed no significant difference.

DISCUSSION

The results of our study show that dynamic SPECT imaging of teboroxime using multidetector SPECT systems can be used to obtain kinetic parameters that are related to coronary blood flow. Using three detectors, sufficient counts with a temporal resolution of 10.2 sec were acquired to model the washin as well as the washout of teboroxime in the heart. It was found that the blood region showing the least extravascular contamination was the superior left-ventricular cavity and the left atrium. The blood time-activity curve generated from this region and the myocardial tissue time-activity curve were fit to an equation which incorporated a parameter f_v that modeled the volume fraction of blood in the tissue and also incorporated a linear two-compartment model consisting of a blood and an extravascular compartment that modeled the washin (k_{21}) and the washout (k_{12}) of teboroxime in the myocardial tissue. The washin parameter k_{21} was significantly ($p < 0.0001$) affected when attenuation correction was performed during the reconstruction process. Also, the washin parameter k_{21} decreased significantly ($p < 0.002$)

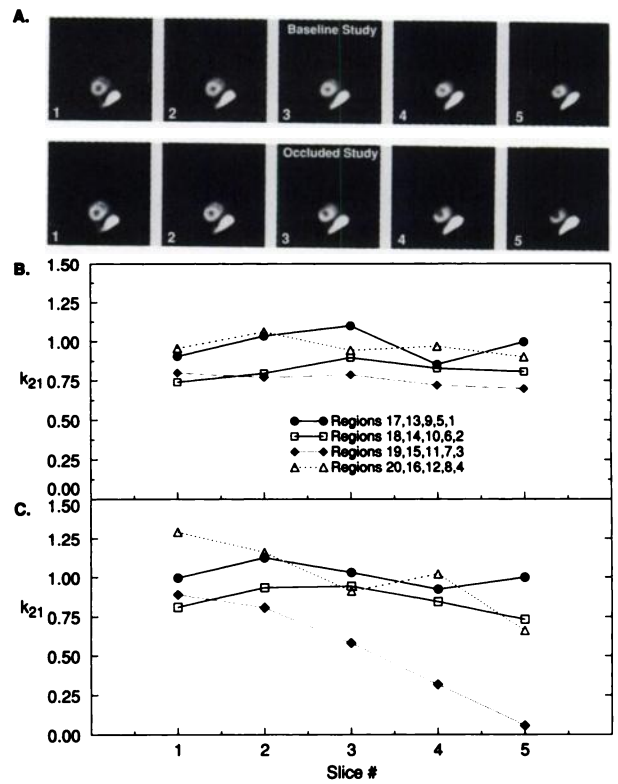

FIGURE 6. (A) Composite short-axis slices of the baseline opened-chest study and the corresponding occluded study (study P3180). The defect was most apparent in regions 11, 7, and 3. (B) The estimated parameter k_{21} from the nonoccluded study plotted as a function of slice number for the various regions. (C) The estimated parameter k_{21} from the occluded study plotted as a function of slice number for the various regions.

when the LAD was occluded, suggesting it may be an indicator of myocardial blood flow.

A major factor limiting the implementation of kinetic modeling using dynamic SPECT imaging is the number of counts that need to be detected in a short time interval. The photon flux of the radiopharmaceutical, the geometric efficiency and the sensitivity of the SPECT system determine the number of counts detected if the effects of attenuation are ignored. The geometric efficiency and detector sensitivity of the SPECT system can be increased by developing new detector technology. The rapidly changing blood input function and the kinetics of the radiopharmaceutical determine the temporal sampling requirements. The photon flux and the kinetics of the radiopharmaceutical can be changed by developing new radiolabeled tracers which maximize these properties.

One improvement that can immediately be made on present multidetector SPECT systems would be to optimize the acquisition of dynamically acquired ^{99m}Tc-teboroxime data. This could be accomplished by implementing variable tomographic acquisition times during the time course of the radiopharmaceutical, thus optimizing the trade-off between temporal sampling requirements of the input function and tomographic data statistics. For example, rapid acquisitions of 5–10 sec for the first 1–2 min of the scan could be acquired, followed by longer acquisitions (30 sec–2 min) as time progressed. Rapid acquisition at the beginning would ensure that the rapidly changing blood compartment is sampled adequately, which reduces the bias in the estimated parameters (*32*). Longer acquisitions can be used after the bolus has dispersed to obtain adequate statistics from the tails of the blood and extravascular time-activity curves when the counts have significantly decreased. More studies need to be done where the acquisition time is varied to determine optimum sampling of the blood and myocardial tissue time-activity curves, along with an accurate analysis of the errors on the fitted parameters to evaluate the various sampling protocols.

Initially, we attempted to select the optimal placement of the blood ROI by comparing time-activity curves generated from various anatomical locations to continuous arterial sampling of the input function from the femoral artery. Unfortunately, the activity in the arterial blood saturated the radiation probe, and the data were unable to be compared to the blood curves generated from the images. We then compared the various blood curves qualitatively and selected the anatomical region based on the following criteria: region with least amount of myocardial tissue spillover (evidenced by higher peaks and lower tail points), region easy to locate on all canine studies, and region large enough for sufficient statistics.

The various anatomical locations investigated were base and apex of the left ventricle, ascending and descending aorta and left atrium. The ascending aorta was difficult to separate from the pulmonary vasculature, while the descending aorta was difficult to locate consistently from study to study. These regions contained at most 2 voxels in a single slice and therefore suffered from problems due to partial volume effects and poor statistics. The regions in the base of the left ventricle and left atrium were chosen because they were anatomically easy to locate due to their large sizes and showed the least amount of spillover from the extravascular compartment as compared to apical regions of the left ventricle. The large size of these regions also minimized partial volume effects.

Later dog studies performed in our lab where the radiation probe was not saturated have shown that as much as 37% of the activity from a blood ROI drawn near the base of the heart actually comes from the tissue. From computer simulations that we have performed (*23*), a 37% spillover of tissue activity into the blood ROI can bias the parameters k_{21} and k_{12} as much as 62.5% and 125%, respectively. More studies need to be done to determine the accuracy of the blood input function generated from the dynamic images. Also note that if an absolute measure of blood flow is desired, an accurate input function is critical (*13,33–35*).

The two-compartment model used to fit the myocardial tissue time-activity curves using the measured blood time-activity curve as the input function was chosen based on the work done in dynamic PET imaging with partially extracted tracers such as ^{82}Rb and $^{16}NH_3$ (*14,15,17,18*). The washin parameter k_{21} in this compartment model is dependent not only on flow but also on the extraction fraction of teboroxime. Rumsey et al. (*36*) showed that the extraction of teboroxime decreased with time due to binding of teboroxime to blood cells and plasma proteins. Teboroxime was highly extracted on the first pass (99.5%), but dropped to 57% after a 5-min extraction.

The decrease in the extraction fraction of teboroxime is a potential problem for accurate quantitation of myocardial blood flow. We performed a computer simulation (*37*) that modeled this binding by assigning a half-life of 5 min for the binding of teboroxime to blood cells and proteins (*36*) and determined that this binding can bias the estimated parameter k_{21} by as much as 50%. In the future, blood samples may need to be drawn (as is done in PET $^{13}NH_3$ studies) to determine the amount of extractable teboroxime in the blood.

Previous computer simulations demonstrated that the washin parameter k_{21} showed the most potential as an indicator of myocardial blood flow. A sensitivity analysis was performed where each parameter (f_v, k_{21} and k_{12}) was changed a set amount for five simulations while holding the other two constant. The extravascular time-activity curve was shown to be relatively insensitive to parameter f_v as compared to parameters k_{21} and k_{12}. The sensitivity analysis also showed that k_{21} exerted its effect on the beginning time points of the extravascular time-activity curve, while k_{12} exerted its effect on the later time points. The results obtained from this study supported the findings from the computer simulations. The %RMS errors for the parameter f_v were consistently the highest, indicating that this parameter had the least precision when fitting the data. The observation that no significant difference occurred in any

of the estimated parameters when 30.6 min of dynamic data were fit as compared to 15.3 min in the closed-chest study indicates that most of the kinetic information is contained in the earlier time points which affect the parameter k_{21} the most. Higher count rates in the extravascular time-activity curves occur during the earlier time points and the %RMS errors for the washin parameter k_{21} were slightly lower than the other parameters for each study, which also indicate that the washin parameter k_{21} may be a more sensitive indicator of blood flow than the washout parameter k_{12}.

The parameter f_v averaged near 34% in these studies which is higher than the quoted literature value of 10%–15% (*38*). Using computer simulations, we determined that the parameter f_v also modeled the averaging of the intraventricular blood activity and myocardial tissue activity due to heart wall motion (*23*), which explains the discrepancy from the literature value. Although this suggests that f_v will have little use in differentiating abnormal from normal tissue, f_v is still important because it models spillover of blood into myocardial tissue due to cardiac motion.

Our studies showed that the estimated parameter k_{21} was significantly influenced if no attenuation correction was used when reconstructing the three-dimensional distribution. The significant change was due in part to the relative attenuation differences between the blood and tissue regions. Thus, attenuation correction is critical when performing kinetic modeling of teboroxime using dynamic SPECT imaging. In addition, attenuation will be more severe in patients; however, the larger heart size in patients will cause less problems due to partial volume effects.

The closed-chest study showed higher uptake of teboroxime in the myocardial tissue which was also reflected in the consistently larger k_{21} and k_{12} values compared to the opened-chest studies. We attribute this finding to different preparations used on the canines. The closed-chest canine was anesthetized with sodium pentobarbital and allowed to breath unassisted. The opened-chest canines were anesthetized with halothane during the imaging and placed on a ventilator. Sodium pentobarbital either increases or has no effect on myocardial blood flow in a canine (*39,40*), whereas halothane has been shown to decrease myocardial blood flow (*40,41*). Spontaneous ventilation compared to controlled ventilation will cause a lower intrathoracic pressure, which would affect hemodynamics and possibly myocardial blood flow as well (*41*).

In the opened-chest studies, the washin parameter k_{21} decreased when baseline regions were compared to their respective occluded regions. However, the exact relationship of k_{21} to absolute blood flow must be established in future studies. If k_{21} is to reflect relative changes in myocardial blood flow, the extraction of teboroxime should not be heavily dependent on blood flow. Stewart et al. (*19*) found that the first pass retention fraction of teboroxime did not change significantly over a wide range of blood flows (0.30–7.70 ml/min/g) in the canine heart. In addition, Chan et al. (*42*) suggested that tracers with a high first-pass myocardial extraction fraction have an initial uptake which is very dependent on blood flow. Teboroxime has a first-pass myocardial extraction fraction of greater than 0.9 (*1,6,38*), which suggests that its kinetics may very well be a good indicator of myocardial blood flow.

Several issues must be addressed before dynamic SPECT imaging of teboroxime can be clinically useful. The optimum camera orbit for thoracic imaging of a patient is a noncircular orbit; however, modern SPECT systems cannot obtain rapid acquisitions in noncircular orbits. Before quantitation of flow in absolute terms is feasible, the effects of cardiac motion, as well as scatter and spatially varying geometric point response which lead to partial volume effects, must be addressed (*13,34,43,44*). Gated dynamic SPECT would decrease problems due to cardiac motion, but low count rates may make it impractical. Finally, the exact relationship of the washin parameter k_{21} to myocardial blood flow must be established.

In summary, this initial study shows promise that a new myocardial perfusion SPECT technique can be developed that closely parallels what has been developed in PET; however, much more work needs to be done to fully understand kinetic modeling of teboroxime using dynamic SPECT imaging. Although kinetic modeling using dynamic PET has many advantages over dynamic SPECT, SPECT offers two significant advantages over PET in terms of cost and availability. Like dynamic PET imaging, dynamic SPECT imaging could be applied to other organs such as the brain and kidney.

ACKNOWLEDGMENTS

The authors thank Ronald H. Huesman, PhD, Pamela G. Coxson, PhD, Gregory J. Klein, MSEE and Thomas F. Budinger, MD, PhD, (Center for Functional Imaging, University of California, Berkeley) for use of their kinetic fitting program. The authors also thank the Biodynamics Research Unit, Mayo Foundation, for use of their software package "Analyze"; Yu-Lung Hsieh, MS and Andy Welch, PhD (Medical Imaging Research Lab, University of Utah Medical Center) for help with the reconstruction software; Scott McJames (Anesthesia Department, University of Utah Medical Center) for his assistance with the canine surgeries; Squibb Diagnostics for supplying the teboroxime; and Picker International for hardware support.

REFERENCES

1. Leppo JA, DePuey EG, Johnson LL. A review of cardiac imaging with sestamibi and teboroxime. *J Nucl Med* 1991;32:2012–2022.
2. Datz FL, Gullberg GT, Gabor FV, Morton KA. SPECT myocardial perfusion imaging update. *Semin Ultrasound CT MR* 1991;12:28–44.
3. Gray W, Gewirtz H. Comparison of ^{99m}Tc-teboroxime with thallium for myocardial imaging in the presence of a coronary stenosis. *Circulation* 1991;844:1796–1807.
4. Hendel RC, McSherry B, Karimeddini M, Leppo JA. Diagnostic value of a new myocardial perfusion agent, teboroxime SQ30217, utilizing a rapid planar imaging protocol: preliminary results. *J Am Coll Cardiol* 1990;16: 855–861.
5. Links JM, Frank TL, Becker LC. Effect of differential tracer washout during SPECT acquisition. *J Nucl Med* 1991;32:2253–2257.
6. Nakajima K, Shuke N, Taki J, et al. A simulation of dynamic SPECT using radiopharmaceuticals with rapid clearance. *J Nucl Med* 1992;33:1200–1206.
7. Huang SC, Phelps ME, Hoffman EJ, Sideris K, Selin CJ, Kuhl DE. Noninvasive determination of local cerebral metabolic rate of glucose in man. *Am J Physiol* 1980;238:E69–E82.

8. Phelps ME, Huang SC, Hoffman EJ, Selin C, Sokoloff L, Kuhl DE. Tomographic measurement of local cerebral glucose metabolic rate in humans with ^{18}F-2-fluoro-2-deoxyglucose: validation of method. *Ann Neurol* 1979; 6:371–388.
9. Reivich M, Alavi A, Wolf A, et al. Use of 2-deoxy-D-1-^{11}C-glucose for the determination of local cerebral glucose metabolism in humans: variation within and between subjects. *J Cereb Blood Flow Metab* 1982;2:307–319.
10. Heiss W-D, Pawlik G, Herholz K, et al. Regional kinetic constants and cerebral metabolic rate for glucose in normal human volunteers determined by dynamic positron emission tomography of ^{18}F-2-fluoro-2-deoxy-d-glucose. *J Cereb Blood Flow Metab* 1984;4:212–223.
11. Sokoloff L, Reivich M, Kennedy C, et al. The [^{14}C]deoxyglucose method for the measurement of local cerebral glucose utilization: theory, procedure and normal values in the conscious and anesthetized albino rat. *J Neurochem* 1977;28:897–916.
12. Budinger TF, Huesman RH, Knittel B, Friedland RP, Derenzo SE. Physiological modeling of dynamic measurements of metabolism using positron emission tomography. In: Greitz T, Ingvar DH, Widen L, eds. *The metabolism of the human brain studied with positron emission tomography*. New York: Raven Press; 1985:165–183.
13. Bergmann SR, Herrero P, Markham J, Weinheimer CJ, Walsh MN. Noninvasive quantitation of myocardial blood flow in human subjects with oxygen-15-labeled water and positron emission tomography. *J Am Coll Cardiol* 1989:14:639–652.
14. Herrero P, Markham J, Shelton ME, Bergmann SR. Implementation and evaluation of a two-compartment model for quantification of myocardial perfusion with rubidium-82 and positron emission tomography. *Circ Res* 1992;70:496–507.
15. Muzik O, Beanlands RSB, Hutchins GD, Mangner TJ, Nguyen N, Schwaiger M. Validation of nitrogen-13-ammonia tracer kinetic model for quantification of myocardial blood flow using PET. *J Nucl Med* 1993;34:83–91.
16. Choi Y, Hawkins RA, Huang SC, et al. Parametric images of myocardial metabolic rate of glucose generated from dynamic cardiac PET and 2-^{18}F-fluoro-2-deoxy-d-glucose studies. *J Nucl Med* 1991;32:733–738.
17. Mullani NA, Goldstein RA, Gould KL, et al. Myocardial perfusion with rubidium-82. I. Measurements of extraction fraction and flow with external detectors. *J Nucl Med* 1983;24:898–906.
18. Goldstein RA, Mullani NA, Marani SK, Fisher DJ, Gould KL, O'Brien, Jr. HA. Myocardial perfusion with rubidium-82. II. Effects of metabolic and pharmacologic interventions. *J Nucl Med* 1983;24:907–915.
19. Stewart RE, Schwaiger M, Hutchins GD, et al. Myocardial clearance kinetics of technetium-99m-SQ30217: a marker of regional myocardial blood flow. *J Nucl Med* 1990;31:1183–1190.
20. Nakajima K, Taki J, Bunko H, et al. Dynamic acquisition with a three-headed SPECT system: application to technetium-99m-SQ30217 myocardial imaging. *J Nucl Med* 1991;32:1273–1277.
21. Budinger T, Araujo L, Ranger N, Coxson P, Huesman R, Alavi A. Dynamic SPECT feasibility studies [Abstract]. *J Nucl Med* 1991;32:955.
22. Smith AM, Gullberg GT, Datz FL, Christian PE. Kinetic modeling of teboroxime using dynamic SPECT imaging [Abstract]. *J Nucl Med* 1992; 38:878–879.
23. Smith AM, Gullberg GT. A dynamic cardiac SPECT computer simulation. *Conference Record of the 1992 IEEE Nuclear Science Symposium and Medical Imaging Conference, volume 2*. Orlando, FL, October 25–31, 1992: 1008–1010.
24. Shepp LA, Vardi Y. Maximum likelihood reconstruction for emission tomography. *IEEE Trans Med Imaging* 1982;MI-1:113–122.
25. Lang K, Carson R. EM reconstruction algorithms for emission and transmission tomography. *J Comp Assist Tomogr* 1984;8:306–316.
26. Gullberg GT, Huesman RH, Malko JA, Pelc NJ, Budinger TF. An attenuated projector-backprojector for iterative SPECT reconstruction. *Phys Med Biol* 1985;30:799–816.
27. Tsui BMW, Gullberg GT, Edgerton ER, et al. Correction of nonuniform attenuation in cardiac SPECT imaging. *J Nucl Med* 1989;30:497–507.
28. Coxson PG, Salmeron EM, Huesman RH, Mazoyer BM. Simulation of compartmental models for kinetic data from a positron emission tomograph. *Comp Meth Prog Biomed* 1992;37:205–214.
29. Huesman RH, Mazoyer BM. Kinetic data analysis with a noisy input function. *Phys Med Biol* 1987;32:1569–1579.
30. Carson RE. Parameter estimation in positron emission tomography. In: Phelps ME, Mazziotta J, Schelbert H, eds. *Positron emission tomography and autoradiography: principles and applications for the brain and heart*. New York: Raven Press; 1986:347–390.
31. Huang S, Phelps ME. Principles of tracer kinetic modeling in positron emission tomography and autoradiography. In: Phelps ME, Mazziotta J, Schelbert H, eds. *Positron emission tomography and autoradiography: principles and applications for the brain and heart*. New York: Raven Press; 1986:287–346.
32. Raylman RR, Caraher JM, Hutchins GD. The effect of temporal sampling on the estimation of kinetic model parameters derived from dynamic PET studies of the heart [Abstract]. *J Nucl Med* 1992;33:881–882.
33. Weinberg IN, Huang SC, Hoffman EJ, et al. Validation of PET-acquired input functions for cardiac studies. *J Nucl Med* 1988;29:241–247.
34. Herrero P, Markham J, Bergmann SR. Quantitation of myocardial blood flow with $H_2^{15}O$ and positron emission tomography: assessment and error analysis of a mathematical approach. *J Comput Assist Tomogr* 1989;13:862–873.
35. Iida H, Rhodes CG, de Silva R, et al. Use of the left ventricular time-activity curve as a noninvasive input function in dynamic oxygen-15-water positron emission tomography. *J Nucl Med* 1992;33:1669–1677.
36. Rumsey WL, Rosenspine KC, Nunn AD. Myocardial extraction of teboroxime: effects of teboroxime interaction with blood. *J Nucl Med* 1992;33:94–101.
37. Smith AM, Gullberg GT, Zeng GL. The accuracy and precision of kinetic parameters estimated from attenuation corrected dynamic SPECT images. Presented at the *IEEE Conference on Medical Imaging*; San Francisco, CA, November, 1993.
38. Morgenstern C, Holjes U, Arnold G, Lochner W. The influence of coronary pressure and coronary flow on intracoronary blood volume and geometry of the left ventricle. *Pflugers Arch* 1973;340:101–111.
39. Manders WT, Vatner SF. Effects of sodium pentobarbital anesthesia on left ventricular function and distribution of cardiac output in dogs, with particular reference to the mechanism for tachycardia. *Circ Res* 1976;39:512–517.
40. Gross DR. *Animal models in cardiovascular research*. Boston: Martinus Nijhoff Publishers; 1985:197–306.
41. Miller RD. *Anesthesia, 2nd edition*. New York: Churchhill Livingstone; 1986:654–666.
42. Chan SY, Brunken RC, Phelps ME, Schelbert HR. Use of the metabolic tracer carbon-11-acetate for evaluation of regional myocardial perfusion. *J Nucl Med* 1991;32:665–672.
43. Hoffman EJ, Huang SC, Phelps ME. Quantitation in positron emission computed tomography: 1. Effect of object size. *J Comput Assist Tomogr* 1979;3:299–308.
44. Ter-Pogossian MM, Bergmann SR, Sobel BE. Influence of cardiac and respiratory motion on tomographic reconstructions of the heart: implications for quantitative nuclear cardiology. *J Comput Assist Tomogr* 1982;6: 1148–1155.